Supporting Information

Direct electrochemical CO_2 conversion using oxygen-mixed gas on a Cu network cathode and tailored anode

Akihiko Anzai,[a] Manabu Higashi,[a] Miho Yamauchi [a,b,c,d,]*

[a] Institute for Materials Chemistry and Engineering (IMCE), Kyushu University, Motooka 744, Nishi-ku, Fukuoka 819-0395, Japan

[b] Advanced Institute for Materials Research (WPI-AIMR), Tohoku University, 2-1-1 Katahira, Aoba-ku, Sendai 980-8577, Japan.

[c] International Institute for Carbon-Neutral Energy Research (WPI-I[2]CNER), Kyushu University, Motooka 744, Nishi-ku, Fukuoka 819-0395, Japan

[d] Research Center for Negative Emissions Technologies (K-Nets), Kyushu University, Motooka 744, Nishi-ku, Fukuoka 819-0395, Japan

* Corresponding Author

Miho Yamauchi; E-mail: yamauchi@ms.ifoc.kyushu-u.ac.jp

Experimental Methods

Materials. Cu wire (purity: >99.999%, 0.5 mmϕ) was purchased from Nilaco Corp. Commercial carbon paper gas diffusion layer (C-GDL) was purchased from Fuel Cell Store (www.fuelcellstore.com, Sigracet® 39 BB PTFE-treated GDL, thickness: 315 microns). Hydrophobic polytetrafluoroethylene (PTFE) membrane filter (T050A047A, diameter: 47 mm, pore size: 0.50 μm, thickness: 75 μm, porosity: 78%) was purchased from Advantec toyo kaisha, ltd. Nafion® 117 cation exchange membrane was purchased from Chemours®. Ni foam (thickness: 1.6 mm, purity >99.99%) was purchased from MTI Corporation. Potassium hydroxide (KOH) and potassium chloride (KCl) were purchased from FUJIFILM Wako Pure Chemical Corporation, and used as received. All the solutions were prepared with deionized water.

Electrode preparation. To deposit a 100-nm-thick copper layer on a typical carbon paper gas diffusion layer (Sigracet 39 BB) (C-GDL) and polytetrafluoroethylene membrane filter (P-GDL), 15 mg of copper wire (approximately 32 mm long) was applied using the thermal evaporator (VPC-260F, Ulvac Kiko. Inc.) at a pressure lower than 4×10^{-3} Pa, and then cooled down to room temperature under vacuum, followed by storage in a vacuum desiccator to avoid oxidation of the copper in the atmosphere.

Characterization. X-ray diffraction (XRD) patterns were obtained on a Bruker D2 Phaser X-ray diffractometer with Ni filtered Cu Kα radiation (λ = 1.5406 Å) at a voltage of 30 kV and a current of 10 mA. Rietveld analyses were performed using a Topas software package (Bruker AXS Inc., Billerica, MA, USA, version 5). Scanning electron microscopy (SEM) images were taken on a JEOL JSM-7900F microscope or JEOL JSM-IT100 microscope. Cu K-edge X-ray absorption fine structure (XAFS) was measured at the Kyushu University beamline BL06 of Kyushu Synchrotron Light Research Center (SAGA-LS, Japan) with an electron storage ring operating at the energy of 1.4 GeV. The energy range of this light source (bending magnet) is 2.1–23 keV. A silicon (111) double-crystal monochromator was used to collect the incident X-ray beam. The typical photon flux is 10^{10} photons per second. All spectra were recorded in the transmission mode at 20 °C using a Si(111) double-crystal monochromator. Data processing was performed using Athena and Artemis included in the Ifeffit package.[1]

Electrochemical measurements. Electrochemical measurements were performed using a three-electrode system in an electrochemical flow cell setup configuration. The cathode in the flow cell has a geometric area of 1 cm^2, which is used for all current density calculations. A flow rate of 4 ml min^{-1} was employed for introducing 1 M KOH or 1 M KCl aqueous solution into the cathode chamber, while a flow rate of 1 mL min^{-1} was used for introducing 1 M KOH aqueous solution into the anode chamber by two pumps, respectively. The cathode camber and anode chamber were separated by a Nafion 117 cation exchange membrane. Pure CO_2 gas (99.99%) or mixed gas containing 40% CO_2, 12% O_2 (>99.5%), and 48%N_2 (>99.9%) was continuously supplied to the gas chamber of the flow cell at a total flow rate of 15 mL min^{-1}. eCO$_2$RR performance was investigated by using constant-potential electrolysis, i.e., chronoamperometry. The potentials versus the Hg/HgO reference electrode were converted to values versus the reversible hydrogen electrode (RHE) using

the following equation[2]:

$$E \text{ (V vs. RHE)} = E \text{ (V vs. Hg/HgO)} + 0.098 \text{ V} + 0.0591 \text{ V} \times pH$$

For the *iR* correction, the uncompensated ohmic resistance of the cathode in the electrolyte solution was determined by potentiostatic electrochemical impedance spectroscopy (PEIS) prior to the chronoamerometric test of the electrode. PEIS was performed at frequencies ranging from 1 MHz to 1 Hz with an amplitude of 10 mV at open circuit potential (OCP).

Gas products were analyzed using on-line gas chromatography (Micro GC Fusion®, Inficon, Bad Ragaz, Switzerland) equipped with a Molsieve 5A column and a Rt-Q-Bond column, and coupled with thermal conductivity detector (TCD). Liquid products were analyzed using a high performance liquid chromatograph (HPLC, LC-20AD, Shimadzu) equipped with a refractive index detector (RID-10A, Shimadzu). The Faradaic efficiency (FE) of products in the electrochemical CO_2 reduction experiments is calculated using the following equation:

$$FE_i = \frac{n_i \times z_i \times F \times 100}{Q},$$

where n_i represents the number of moles of product i, and z_i represents the number of electrons required for the formation of product i (z_i = 2 for CO, formic acid, and H_2; z_i = 8 for CH_4; z_i = 12 for C_2H_4; z_i = 18 for C_3H_7OH). F is the Faraday constant which has a value of 96,485 C mol^{-1} of electrons. Q represents the total charge passed during the electrolysis. For the gas products, n_i was calculated using the following equation:

$$n_i = \frac{P_0 \times x_i \times v \times t}{R \times T},$$

where x_i represents the volume fraction of gas product i, and P_0 represents the atmospheric pressure (1 atm). v represents the CO_2 flow rate (0.015 L min^{-1}). t represents electrolysis time. R represents the ideal gas constant (0.08205 L atm mol^{-1} K^{-1}). T represents the temperature 298 K.

Table S1. Standard potentials for electrochemical CO_2 reduction (eCO_2R), hydrogen evolution reaction (HER), and oxygen reduction reaction (ORR).[3,4,5]

Half reaction	E_0 (V vs. RHE)
$CO_2 + H_2O + 2e^- \rightarrow CO + 2OH^-$	−0.932
$CO_2 + H_2O + 2e^- \rightarrow HCOO^- + OH^-$	−0.639
$CO_2 + 6H_2O + 8e^- \rightarrow CH_4 + 8OH^-$	−0.659
$2CO_2 + 5H_2O + 8e^- \rightarrow CH_3COO^- + 7OH^-$	−0.653
$2CO_2 + 9H_2O + 12e^- \rightarrow C_2H_5OH + 12OH^-$	−0.744
$2CO_2 + 8H_2O + 12e^- \rightarrow C_2H_4 + 12OH^-$	−0.743
$3CO_2 + 13H_2O + 18e^- \rightarrow C_3H_7OH + 18OH^-$	−0.733
$2H_2O + 2e^- \rightarrow H_2 + 2OH^-$	−0.828
$O_2 + H_2O + 4e^- \rightarrow 4OH^-$	0.401
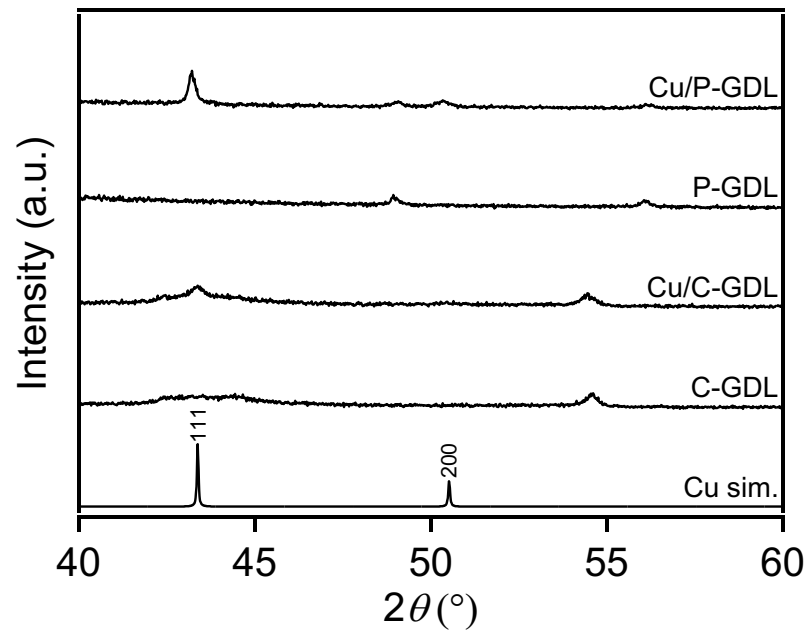
Fig. S1. XRD patterns of C-GDL, Cu/C-GDL, P-GDL, Cu/P-GDL, and Cu.

In XRD patterns of Cu/C-GDL and Cu/P-GDL, we found broad peaks at 43.7 and 50.3 °, which were indexed to (111) and (200) reflections of face-centered cubic Cu, and the other peaks, corresponding to those of bare C-GDL or P-GDL.
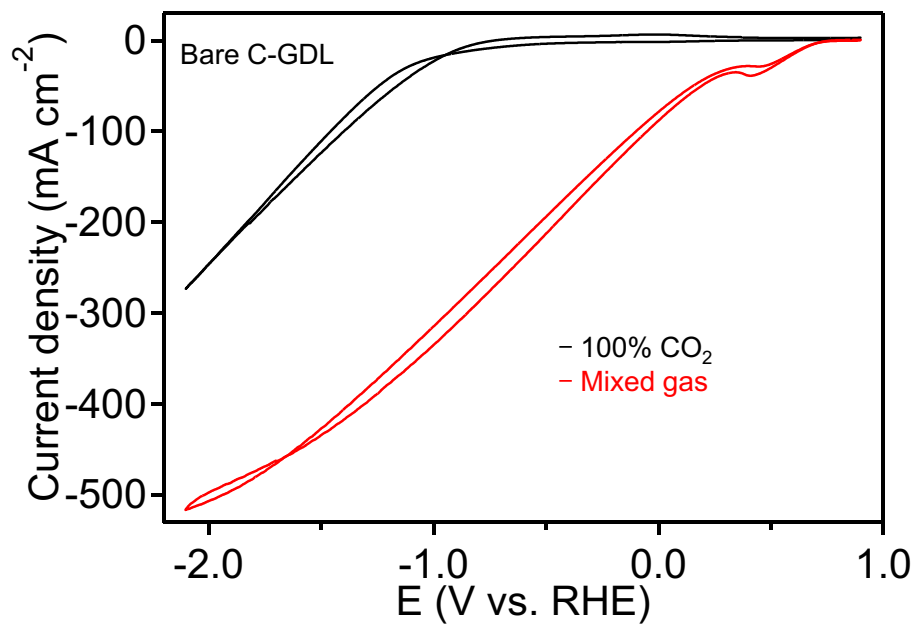
Fig. S2 CV curves of the eCO$_2$R without *iR* compensation on bare C-GDL (commercial GDLs, 39 BB from SIGRACET®) in 1 M KOH under 100% CO$_2$, and 40% CO$_2$, 12% O$_2$, and 48% N$_2$ at 50 mV s^{-1}.

Table S2. List of onset potentials (vs. RHE) estimated from cyclic voltammograms of Cu/C-GDL, Cu/P-GDL, Ag/P-GDL, and C-GDL in 1 M KOH under 100% CO_2, and 40% CO_2 mixed gas.

GDE	100% CO_2	Mixed gas
Cu/C-GDL	−0.30	0.70
Cu/P-GDL	−0.40	0.33
Ag/P-GDL	−0.55	0.46
C-GDL	−0.50	0.72
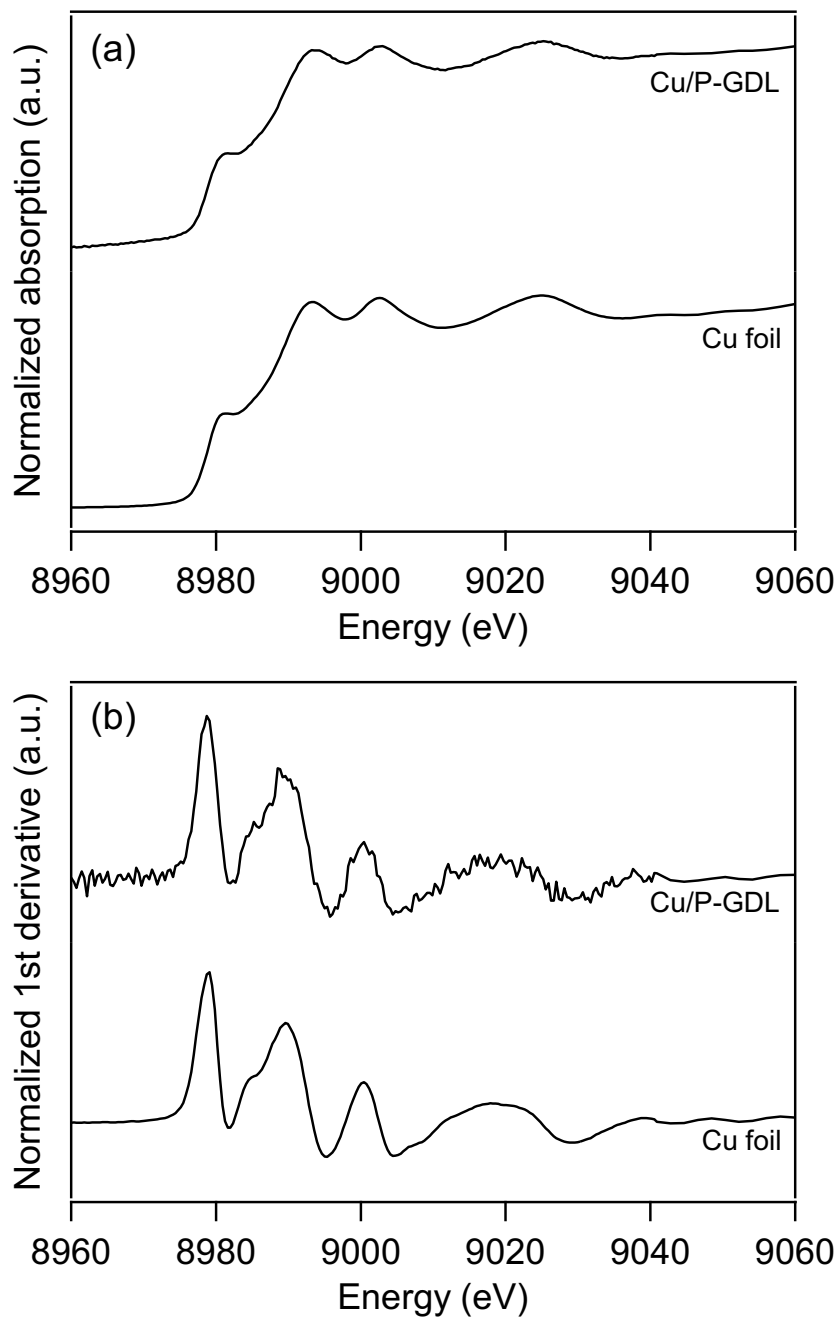
Fig. S3 Cu K edge XANES spectra of the Cu/P-GDL and Cu foil as a reference (a), and the corresponding 1st derivative spectra.
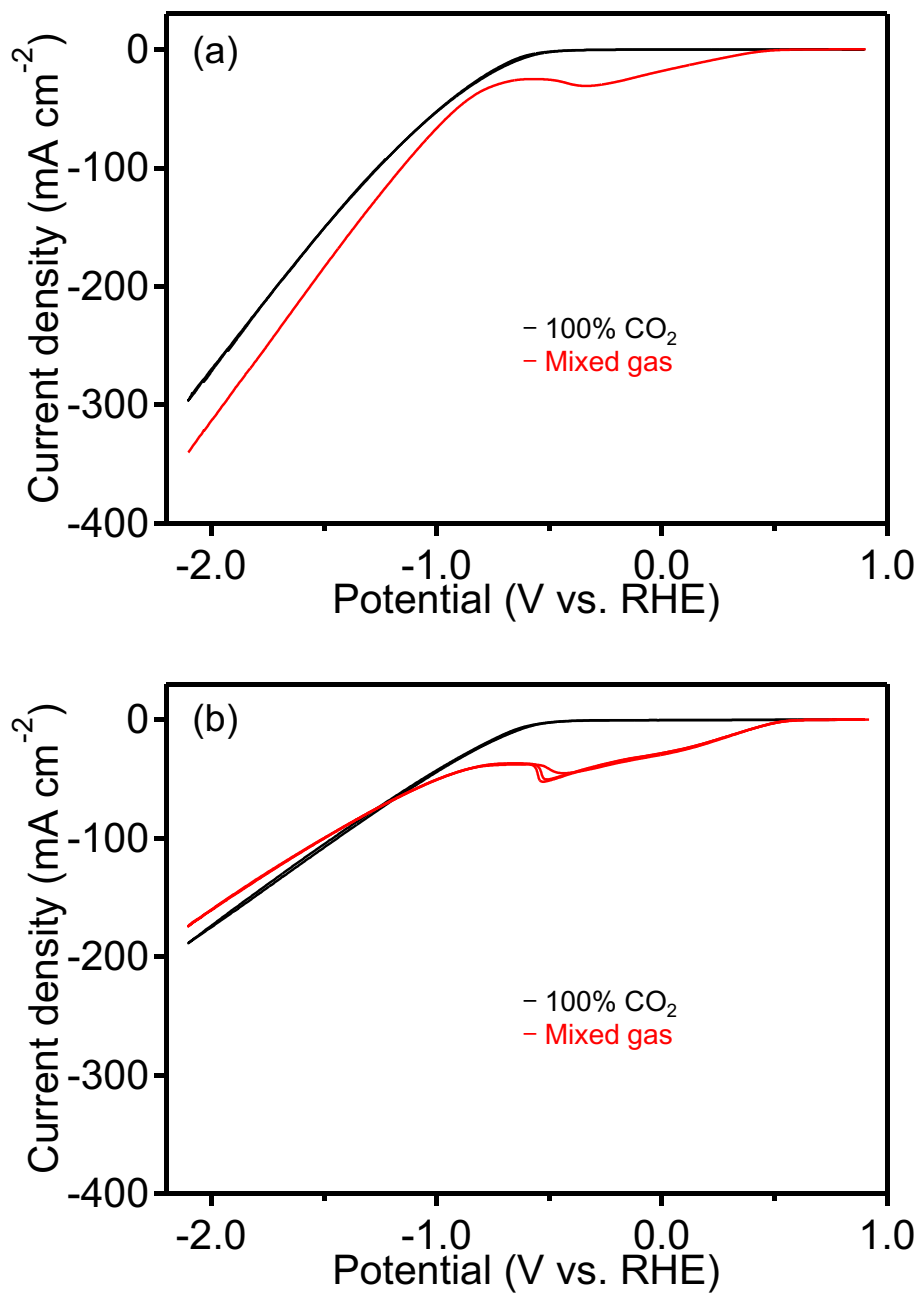
Fig. S4. CV curves of the Ag/P-GDL without iR compensation in 1 M KOH (a) or 1 M KCl (b) under 100% CO_2 and mixed gas at 50 mV s^{-1}.

Table S3. Faradaic efficiency data at different potentials without *iR* compensation on Cu/C-GDL in 1 M KOH under 100% CO_2.

E (V vs. RHE)	Current density (mA cm^{-2})	Faradaic efficiency (%)							
		H_2	HCOOH	CO	CH_4	C_3H_7OH	CH_3CO_2H	C_2H_5OH	C_2H_4
−1.2	139.4	14.5	4.7	10.0	1.9	2.8	2.0	19.0	44.8
−1.0	92.2	14.9	6.9	13.4	1.7	0.0	1.7	15.3	40.8
−0.8	50.6	16.6	7.0	20.1	0.0	0.0	1.8	10.4	34.2

Table S4. Faradaic efficiency data at different potentials without *iR* compensation on Cu/C-GDL in 1 M KOH under mixed gas.

E (V vs. RHE)	Current density (mA cm^{-2})	Faradaic efficiency (%)							
		H_2	HCOOH	CO	CH_4	C_3H_7OH	CH_3CO_2H	C_2H_5OH	C_2H_4
−1.2	301.7	0.0	0.0	0.0	0.0	0.0	0.0	0.0	0.0
−1.0	262.3	0.0	0.0	0.0	0.0	0.0	0.0	0.0	0.0
−0.8	223.1	0.0	0.0	0.0	0.0	0.0	0.0	0.0	0.0

Table S5. Faradaic efficiency data at different potentials without *iR* compensation on Cu/P-GDL in 1 M KOH under 100% CO_2.

E (V vs. RHE)	Current density (mA cm^{-2})	Faradaic efficiency (%)							
		H_2	HCOOH	CO	CH_4	C_3H_7OH	CH_3CO_2H	C_2H_5OH	C_2H_4
−1.2	152.4	4.1	1.3	8.1	0.6	6.2	2.4	26.7	50.9
−1.0	98.4	4.6	1.5	11.9	0.6	7.6	1.5	23.5	50.0
−0.8	50.1	7.0	2.4	19.9	0.0	9.1	2.5	13.6	46.7

Table S6. Faradaic efficiency data at different potentials without *iR* compensation on Cu/P-GDL in 1 M KOH under mixed gas.

E (V vs. RHE)	Current density (mA cm^{-2})	Faradaic efficiency (%)							
		H_2	HCOOH	CO	CH_4	C_3H_7OH	CH_3CO_2H	C_2H_5OH	C_2H_4
-1.2	151.6	10.9	0.4	1.4	0.5	2.9	2.8	25.1	34.6
-1.0	104.0	5.2	0.3	3.1	0.0	5.3	2.2	22.3	36.8
-0.8	60.3	3.8	0.2	5.6	0.0	7.5	3.4	21.9	26.7

Table S7. Faradaic efficiency data at different potentials with *iR* compensation on Cu/P-GDL in 1 M KOH under mixed gas.

E (V vs. RHE)	Current density (mA cm^{-2})	Faradaic efficiency (%)							
		H_2	HCOOH	CO	CH_4	C_3H_7OH	CH_3CO_2H	C_2H_5OH	C_2H_4
-0.65	151.6	10.9	0.4	1.4	0.5	2.9	2.8	25.1	34.6
-0.62	104.0	5.2	0.3	3.1	0.0	5.3	2.2	22.3	36.8
-0.58	60.3	3.8	0.2	5.6	0.0	7.5	3.4	21.9	26.7

Table S8. Faradaic efficiency data at different potentials with *iR* compensation on Cu/P-GDL in 1 M KCl under mixed gas.

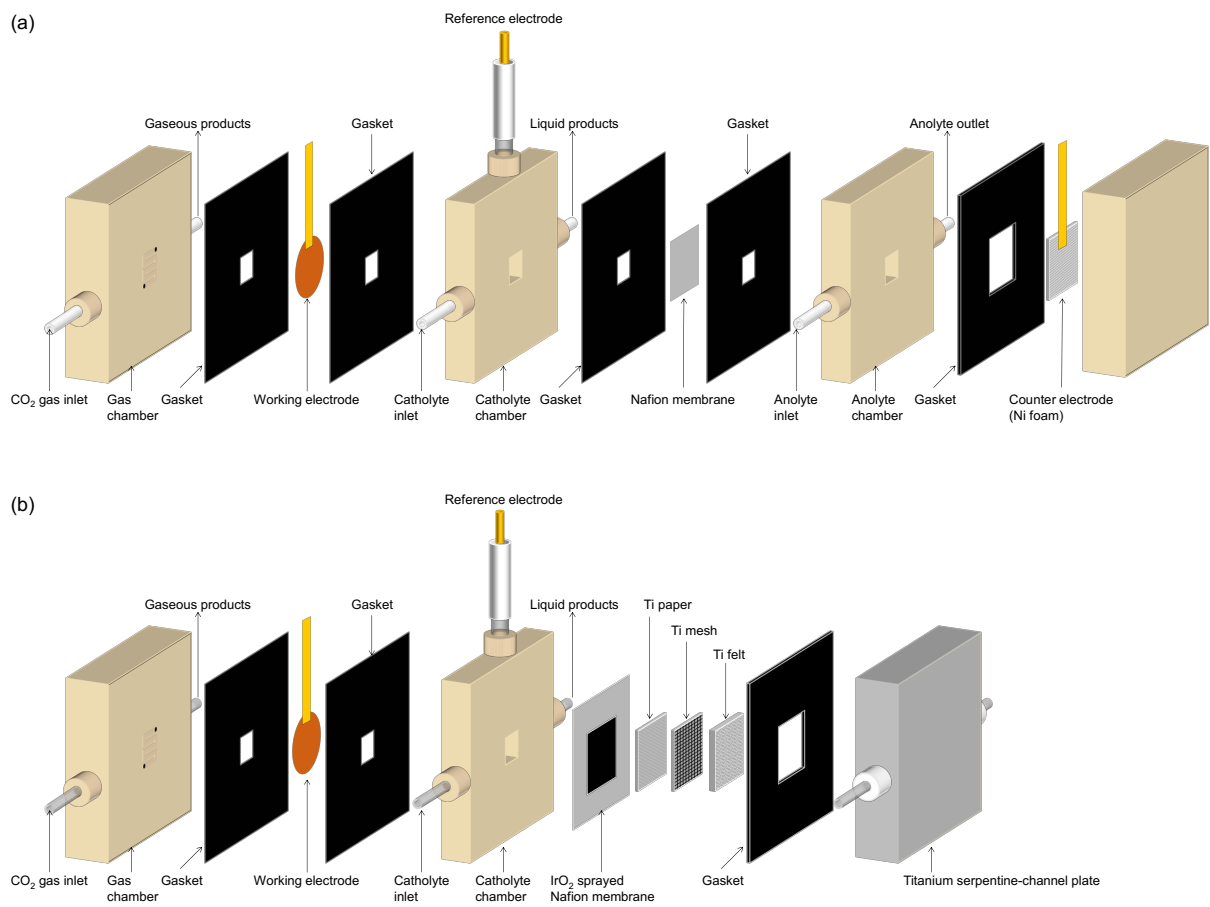| E (V vs. RHE)	Current density (mA cm^{-2})	Faradaic efficiency (%)							
		H$_2$	HCOOH	CO	CH$_4$	C$_3$H$_7$OH	CH$_3$CO$_2$H	C$_2$H$_5$OH	C$_2$H$_4$
-0.61	94.3	14.6	0.8	0.8	11.9	2.8	3.0	29.7	33.6
-0.55	71.5	4.8	1.4	2.2	3.0	2.0	2.7	22.7	39.7
-0.51	47.0	3.9	2.5	5.2	4.4	1.7	2.6	24.7	34.1

Table S9. Faradaic efficiency data at different potentials with *iR* compensation on Ag/P-GDL in 1 M KOH under mixed gas.

| E (V vs. RHE)	Current density (mA cm^{-2})	Faradaic efficiency (%)							
		H$_2$	HCOOH	CO	CH$_4$	C$_3$H$_7$OH	CH$_3$CO$_2$H	C$_2$H$_5$OH	C$_2$H$_4$
-0.92	125.5	89.0	1.1	3.0	0	0	0	0	0
-0.74	69.0	64.6	1.4	7.1	0	0	0	0	0
-0.67	33.5	18.9	2.8	9.7	0	0	0	0	0

Table S10. Faradaic efficiency data at different potentials with *iR* compensation on Ag/P-GDL in 1 M KCl under mixed gas.

| E (V vs. RHE)	Current density (mA cm^{-2})	Faradaic efficiency (%)							
		H_2	HCOOH	CO	CH_4	C_3H_7OH	CH_3CO_2H	C_2H_5OH	C_2H_4
−0.96	168.8	6.6	41.6	26.9	0	0	0	0	0
−0.88	125.3	1.5	23.5	39.1	0	0	0	0	0
−0.81	80.4	0.1	8.0	40.8	0	0	0	0	0

(a)

Reference electrode

Gaseous products   Gasket   Liquid products   Gasket   Anolyte outlet

CO_2 gas inlet   Gas chamber   Gasket   Working electrode   Catholyte inlet   Catholyte chamber   Gasket   Nafion membrane   Anolyte inlet   Anolyte chamber   Gasket   Counter electrode (Ni foam)

(b)

Reference electrode

Gaseous products   Gasket   Liquid products   Ti paper   Ti mesh   Ti felt

CO_2 gas inlet   Gas chamber   Gasket   Working electrode   Catholyte inlet   Catholyte chamber IrO_2 sprayed Nafion membrane   Gasket   Titanium serpentine-channel plate

Fig. S5. Schematic of the a microfluidic cell (a) and a hybrid cell (b), which incorporates the microfluidic cell and MEA, used in this work. The total geometric area of the flow field in the cathode (electrode active area) is 1 cm^2.
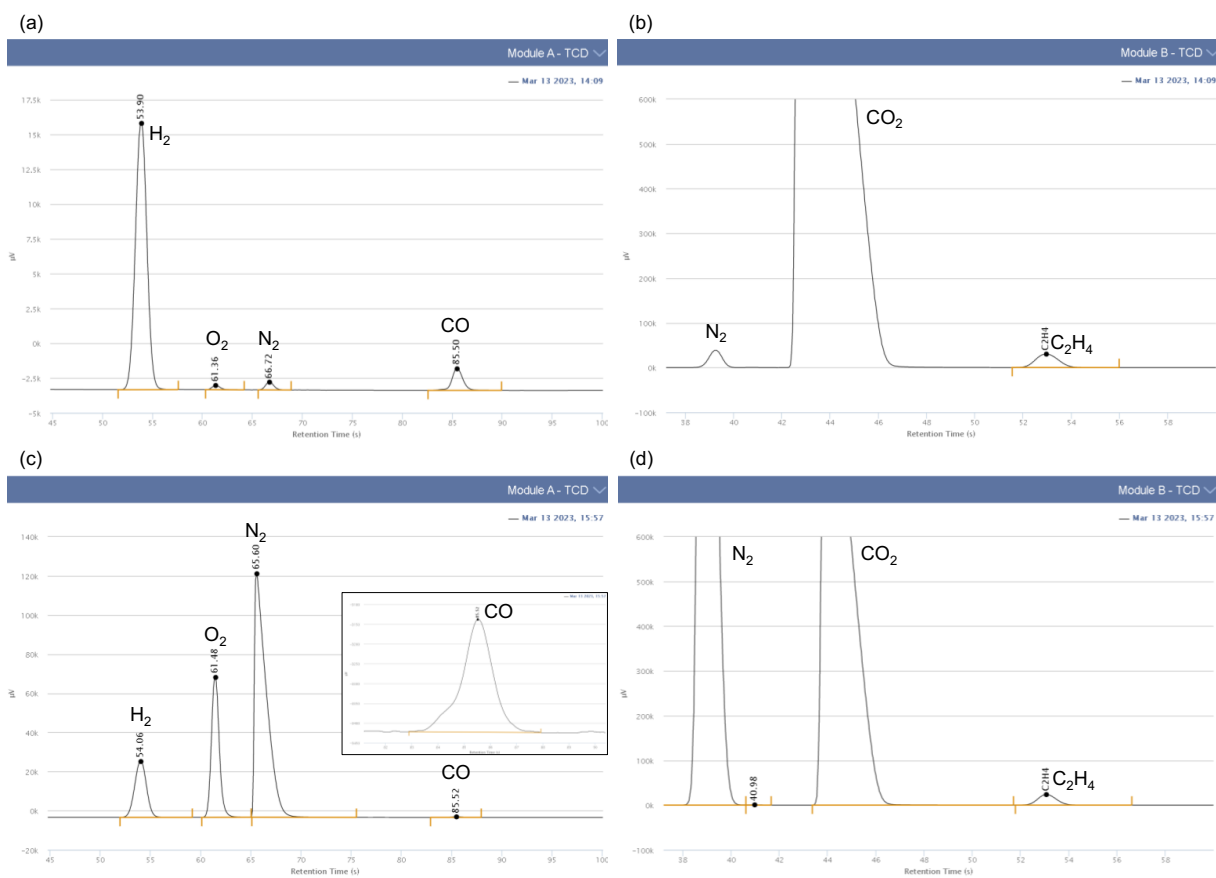
Fig. S6. Examples of gas chromatogram of H_2, O_2, N_2, CO, CO_2, and C_2H_4 obtained by eCO_2R at -0.70 V vs. RHE with *iR* compensation in 1 M KOH under 100% CO_2 (a)(b), and 40% CO_2 mixed gas (c)(d) using Cu/P-GDL cathode. Fig.S6a and Fig.S6c display chromatograms generated using a Rt-Molsieve 5A column channel with argon as carrier gas. Fig.S6b and Fig.S6d display chromatograms generated using a Rt-Q-Bond column channel with helium.
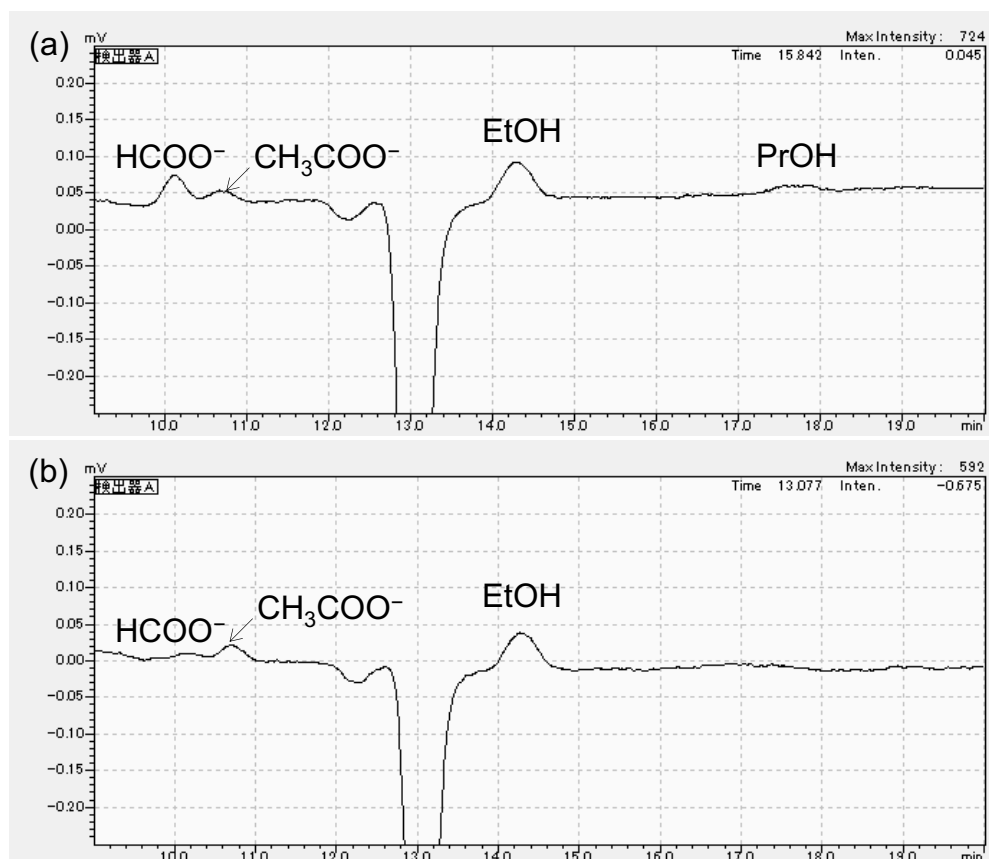
Fig. S7. Example of a high-performance liquid chromatography (HPLC) chromatogram of liquid products obtained by eCO$_2$R at −0.70 V vs. RHE with iR compensation in 1 M KOH under 100% CO$_2$ (a), and 40% CO$_2$ mixed gas (b) using Cu/P-GDL cathode.
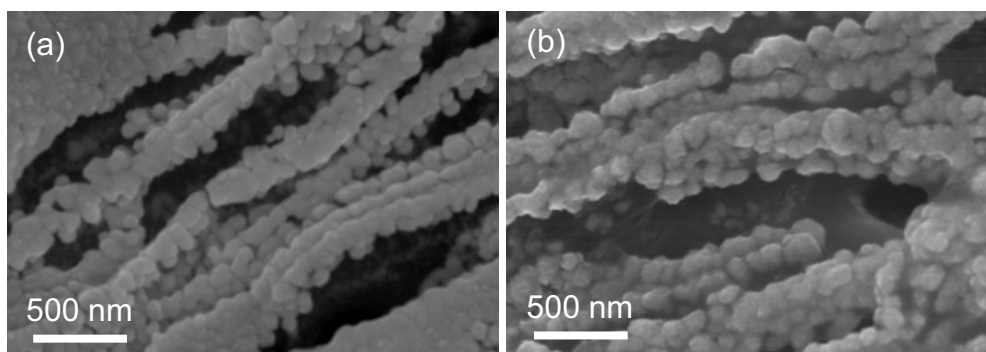
Fig. S8. SEM images of Cu/P-GDL before (a) and after(b) electrolysis under mixed gas at −0.70 V vs. RHE with *iR* compensation in 1 M KOH for 2 hour.

SEM images of the Cu/P-GDL after the reaction (Fig. S9b) revealed that the Cu nanoporous network structure formed on P-GDL consists of Cu aggregates with sizes in the range of hundreds of nanometers, similar to those seen before the reaction (Fig. 2b and Fig. S9a). This observation suggests that Cu on P-GDL retains its structural stability during the reaction at –0.70 V vs. RHE for 2 h. The inherent structural stability of Cu on P-GDL accounts for the stable current response depicted in Fig. 4d.
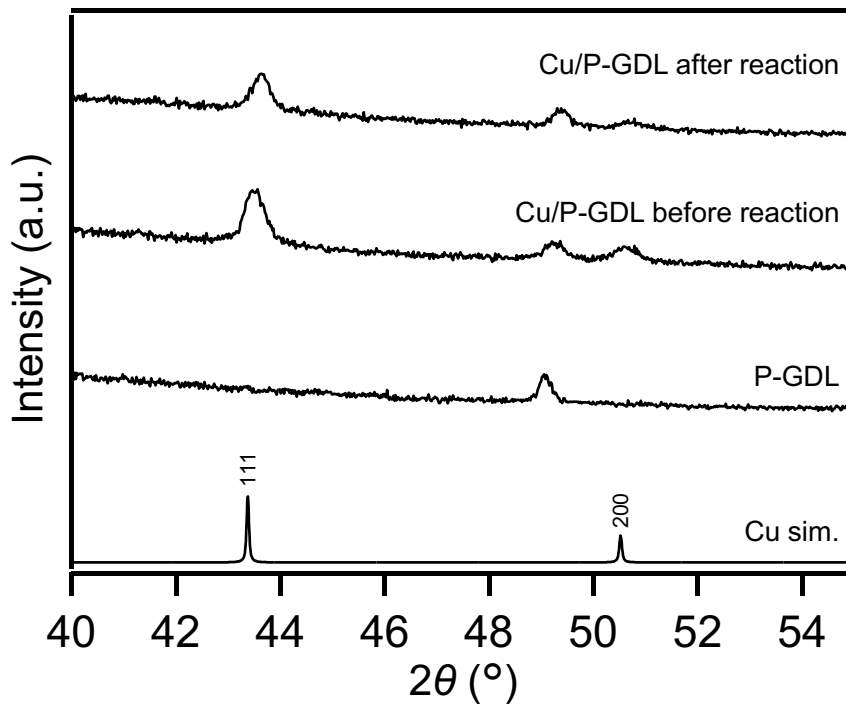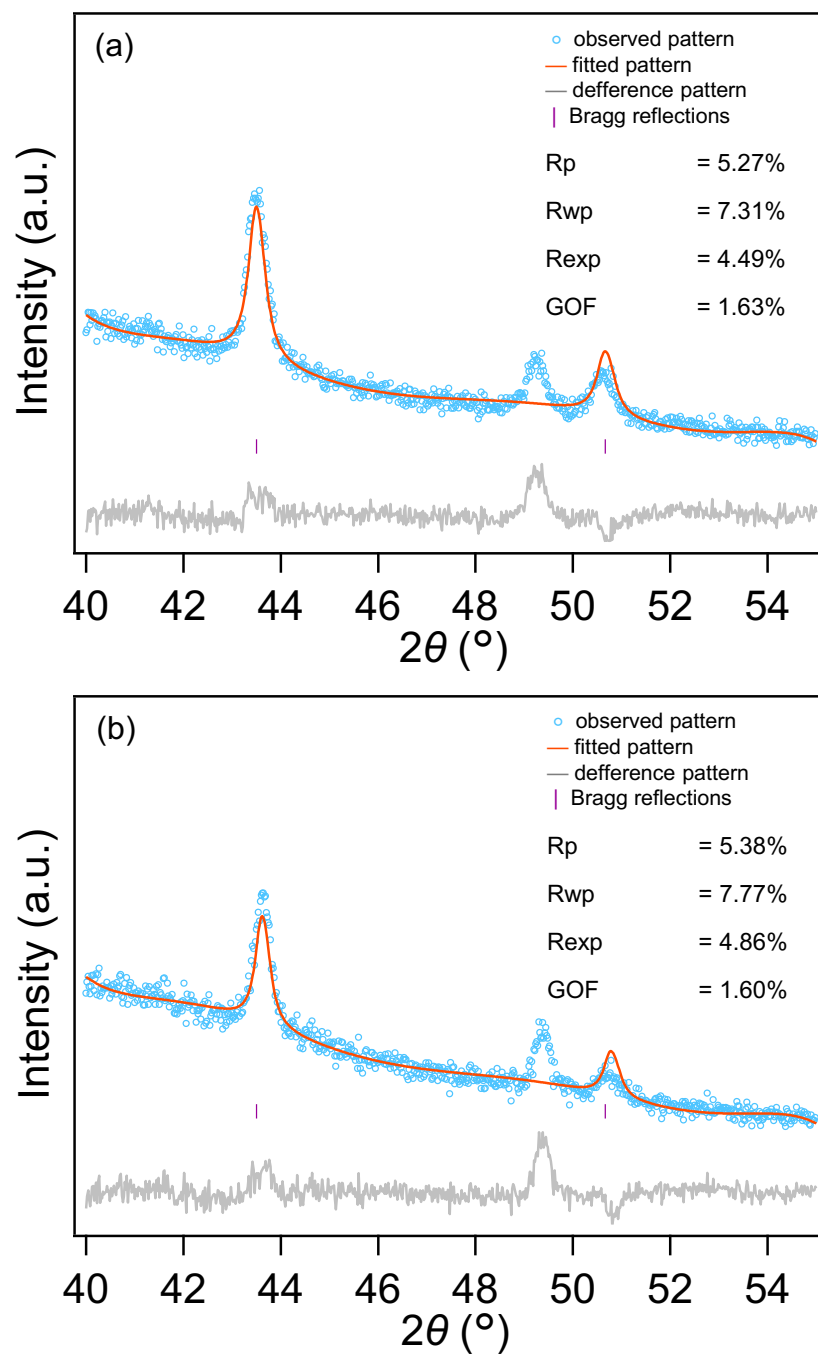
Fig. S9. XRD patterns of Cu/P-GDL before (a) and after (b) electrolysis under mixed gas at −0.70 V vs. RHE with *iR* compensation in 1 M KOH for 2 hour.

In XRD patterns of Cu/P-GDL both before and after electrolysis under mixed gas, we found broad peaks at 43.7 and 50.3°, which were indexed to (111) and (200) reflections of face-centered cubic Cu, and the peak at 49.1°, corresponding to PTFE constitutes bare P-GDL.

Fig. S10. Rietveld analysis results for XRD pattern for Cu/P-GDL before (a) and after (b) electrolysis. Data points are shown as light blue circles and fitted pattern as a red continuous line and the difference between both as a gray line. Bragg positions for fcc copper phase are given in purple dashes.

Table S11. Crystallographic data and Rietveld refinement parameters of Cu/P-GDL before and after electrolysis under 40% CO_2 mixed gas at −0.70 V vs. RHE with *iR* compensation in 1 M KOH for 2 hour.

	before reaction	after reaction
Crystal system	cubic	cubic
Space group	Fm-3m	Fm-3m
a (Å)	3.602	3.601
V (Å^3)	46.75	46.7
crystallite size (nm)	27.4	33.4
T (K)	298	298
Rp	5.27	5.38
Rwp	7.31	7.77
Rexp	4.49	4.86
GOF	1.63	1.60
2θ range	40-55°	40-55°
wavelength (Å)	1.5405	1.5405

To acquire detailed structural parameters for the Cu on the P-GDL both before and after the reaction, we performed Rietveld profile fitting on the XRD patterns (Fig. S10). The obtained structural parameters were compiled and presented in Table S11. The lattice constants of the face-centered cubic (fcc) Cu phase exhibited no discernible alteration before and after the reaction. The crystallite size of Cu before and after the reaction was estimated to be 27 and 33 nm, respectively. These results suggest that Cu/P-GDL exhibited structural stability during electrolysis for 2h in 1 M KOH under mixed gas.

Table S12. The summary of products generation from eCO$_2$R under O$_2$-containing CO$_2$ gas.

Electrocatalyst	Reactor type	Electrolyte	Separator	Anode	E (V)	O$_2$ (vol%)	Pressure (bar)	Main product	FEi	ji (mA cm^{-2})	Ref.
PIM-CoPc/CNT	Flow cell	0.5 M KHCO$_3$	Selemion DSV	CoO$_x$/CNT	3.1 (cell)	5	1	CO	75.9	20.7	6
PIM-CoPc/CNT	Flow cell	0.5 M KHCO$_3$	Selemion DSV	CoO$_x$/CNT	3.1 (cell)	20	1	CO	49.7	14.2	6
DEA-SnOx/C	H-type	0.5M KHCO$_3$		Pt wire	−0.75 (vs. RHE)	8	1	HCOOH	84.2	6.7	7
Sustainion/TiO$_2$/Cu-PTFE	Flow cell	1M KOH		Ni foam	3.0 (cell)	4	10	C$_{2+}$	48.2	126	8
Sustainion/TiO$_2$/Cu-PTFE	Flow cell	1M KOH		Ni foam	3.0 (cell)	4	1	C$_{2+}$	3.7	13.0	8
Sn/PIM/aniline	Flow cell	0.5 M KHCO$_3$	Selemion DSV	NiFe-LDH	−2.4 (vs. Ag/AgCl)	5	1	HCOOH	100	56.7	9
CoPc/CNT/PIM/aniline	Flow cell	0.5 M KHCO$_3$	Selemion DSV	CoO$_x$/CNT	−2.8 (vs. Ag/AgCl)	10	1	CO	71	21.7	9
Cu	H-type	0.1 M CO$_2$-saturated KHCO$_3$	Selemion AMV		−1.0 (vs. RHE)	10	1	C$_{2+}$	10.9	7.3	10
Ag	H-type	0.1 M CO$_2$-saturated KHCO$_3$	Selemion AMV		−0.7 (vs. RHE)	20	1	CO	8.8	8.2	11
Ag/PTFE/MMM PGDE	Flow cell	1 M KHCO$_3$	Fumasep FBM-PK	Ni foam	−1.52 (vs. RHE)	4	1	CO	30	64	12
Cu/P-GDL	**Flow cell**	**1M KOH**	**Nafion 117**	**Ni foam**	**−0.71 (vs. RHE)**	**12**	**1**	**C$_{2+}$**	**85**	**132**	**This work**
Ag/P-GDL	**Flow cell**	**1M KCl**	**Nafion 117**	**Ni foam**	**−0.96 (vs. RHE)**	**12**	**1**	**HCOOH**	**42**	**70**	**This work**
Ag/P-GDL	**Flow cell**	**1M KCl**	**Nafion 117**	**Ni foam**	**−0.88 (vs. RHE)**	**12**	**1**	**CO**	**39**	**49**	**This work**

References

1   B. Ravel and M. Newville, *J. Synchrotron Radiat.*, 2005, **12**, 537–541.

2   S. Niu, S. Li, Y. Du, X. Han and P. Xu, *ACS Energy Lett.*, 2020, **5**, 1083–1087.

3   L. Fan, C. Xia, F. Yang, J. Wang, H. Wang and Y. Lu, *Sci. Adv.*, 2020, **6**, 1–18.

4   X. Ge, A. Sumboja, D. Wuu, T. An, B. Li, F. W. T. Goh, T. S. A. Hor, Y. Zong and Z. Liu, *ACS Catal.*, 2015, **5**, 4643–4667.

5   S. G. Bratsch, *J. Phys. Chem. Ref. Data*, 1989, **18**, 1–21.

6   X. Lu, Z. Jiang, X. Yuan, Y. Wu, R. Malpass-Evans, Y. Zhong, Y. Liang, N. B. McKeown and H. Wang, *Sci. Bull.*, 2019, **64**, 1890–1895.

7   Y. Cheng, J. Hou and P. Kang, *ACS Energy Lett.*, 2021, **6**, 3352–3358.

8   Y. Xu, J. P. Edwards, J. Zhong, C. P. O'Brien, C. M. Gabardo, C. McCallum, J. Li, C. T. Dinh, E. H. Sargent and D. Sinton, *Energy Environ. Sci.*, 2020, **13**, 554–561.

9   P. Li, X. Lu, Z. Wu, Y. Wu, R. Malpass-Evans, N. B. McKeown, X. Sun and H. Wang, *Angew. Chem., Int. Ed.*, 2020, **59**, 10918–10923.

10   M. He, C. Li, H. Zhang, X. Chang, J. G. Chen, W. A. Goddard, M. jeng Cheng, B. Xu and Q. Lu, *Nat. Commun.*, 2020, **11**, 3844.

11   C. Li, H. Xiong, M. He, B. Xu and Q. Lu, *ACS Catal.*, 2021, **11**, 12029–12037.

12   T. Al-Attas, S. K. Nabil, A. S. Zeraati, H. S. Shiran, T. Alkayyali, M. Zargartalebi, T. Tran, N. N. Marei, M. A. Al Bari, H. Lin, S. Roy, P. M. Ajayan, D. Sinton, G. Shimizu and M. G. Kibria, *ACS Energy Lett.*, 2023, **8**, 107–115.